International Journal of Control and Automation
Vol.8, No.3 (2015), pp.217-232
http://dx.doi.org/10.14257/ijca.2015.8.3.23

High-Order Control System Pole-zero Optimal Configuration

Xiaoxuan Chen [1], Wenjuan Li [1], Lijiao Gong [2] and Xudong Chen [3]

[1] *College of chemistry and chemical engineering, Shihezi University, Shihezi, P. R. China*
[2] *College of Machinery and Electrical Engineering, Shihezi University, Shihezi, P.R.* China
[3] *Printing Engineering Department, Anhui Press and Publication Vocational College, Hefei, P.R. China*
cxx19950205@sina.com (Xudong Chen)

Abstract

During the design process of the DC motor composite positioning control system (CPCS), in order to solve the contradiction between the positioning accuracy and the stability, we introduce the equioscillation and equiprecision lines in the root locus plane, analyze and compare root locus maps, the frequency characteristics, and the dynamic responses for PID and CPCS on MATLAB. The results show: within the high-order control system root locus configuration boundary, there always exist three specific boundaried subspaces. Under the condition of simplifying the transferring function to fifth-order from using zero, poles cancellation method, the subspaces' controllability and observability are not changed. The determination of status feedback matrix K and estimator gain L for the high-order control system can be transformed to solving the third-order dynamic equations for specific boundary conditions, and by constructing the dynamic regulator or compensator achieve zero-pole optimal configuration.

Keywords: *High-order control system; Dynamic performance; Positioning accuracy; Positioning stability; Equioscillation line; Equiprecision line*

1. Introduction

Due to the constantly increasing demands on precision control and stability, composite, nonlinear, and other high-order control systems have been widely used in industry [1]. In order to increase, decrease, or change zero pole positions according to design expectations, and achieve the objectives of enhanced control accuracy and improved system structure, the system status feedback gain matrix *K* and the estimator gain matrix *L* should be analyzed quantitatively [2]. Unfortunately, high-order control system transfer function simplification may cause changes in state variables [3], resulting in the generation of uncontrollable and unobservable subspaces [4]. As a result, the determination of system dynamic performance tends to be complex [5], and the establishment of zero-pole configurable conditions and the solution to the status feedback gain matrix would be tedious [6]. Currently, matching approximation methods such as iteration and trial and error are most widely adopted [7].

In this paper we analyze the influences of various pole and zero position distribution changes to system dynamic performance in an attempt to find the precise mathematical solutions to the high-order control systems status feedback gain matrix and the estimator gain matrix. Using these we can achieve zero-pole optimal configuration.

ISSN: 2005-4297 IJCA

2. DC Motor Composite Positioning Control System Design

2.1. DC Motor Composite Positioning Control System Construction

Characteristic and Bode diagram analysis showed that the piezoelectric ceramic micro displacement positioning control system (PZT) and the proportional-integral-derivative controller (PID) exhibited strong complementary functions in the DC motor positioning control process [8]. Taking advantage of this, we constructed a DC motor composite positioning control system. The result is shown in Figure 1.

In order to increase the effective positioning reference displacement of PZT to approximately ± 0.1 mm, piezoelectric ceramics employed 50 cascaded piezoelectric stacks [9]. In order to reduce the piezoelectric stacks' hysteresis, creep, and nonlinear effects, PZT adopted displacement feedback close-loop control [10], which resulted in linear displacement of the feedback signal. The 1 mm high precision lead screw in Figure 1 was used to alternate the angular output of the DC motor to linear displacement and input it into the piezoelectric stack. After they were converted to electrical signals and compared in the position controller, the real and reference displacement signals coming from the piezoelectric stack were exported to the piezoelectric stack controller. From there, signals were finally sent back to the piezo stack to form a feedback close-loop through high-frequency filtering and current-limit handling.

The PID controller adopted a dual closed-loop feedback incremental algorithm [11]. The inner loop was a current loop and the outer loop was composed of position and speed loops. In order to improve control precision, a 20 Hz low pass filter was used to filtrate the feedback signals between the outer and inner rings.

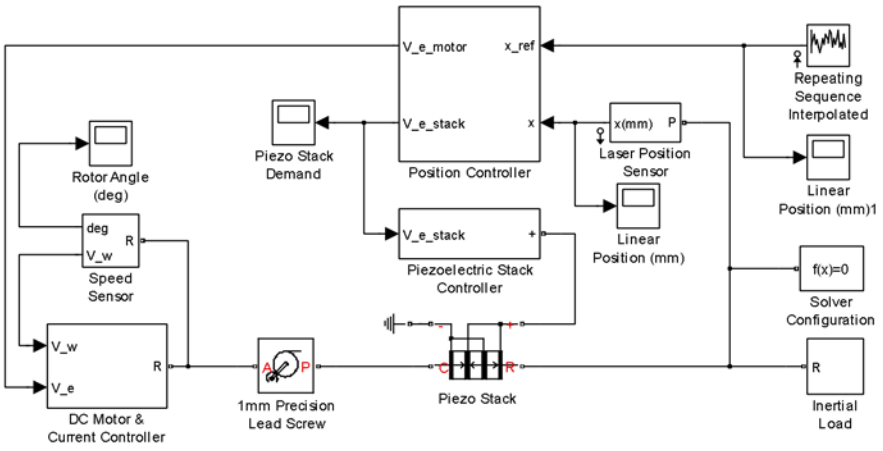

Figure 1. DC Motor Composite Positioning Control System Model

Taking 10mm and 0.05mm unit step pulses as two kinds of positioning reference displacement signals, we tested PID and CPCS's positioning effects. Position and velocity responses are shown in Figure 2.

Figure 2 (a) and (c) show the positioning responses of the PID and CPCS respectively in response to two different signals. It was observed that when the positioning reference displacement was greater than the piezoelectric effective positioning displacement (Figure 2(a)), CPCS's positioning effect was decided only by the PID. Conversely, when the positioning reference displacement was less than the effective positioning displacement of PZT (Figure 2(b)), CPCS automatically switched, turning off PID and instead starting PZT

for location. The overshoot and maximum positioning time of CPCS were much smaller than those for PID, and positioning accuracy was significantly improved. These results met our design expectations well. However, we found that CPCS's speed experienced oscillation at the beginning of the control process under both positioning signals, showing a certain degree of instability when compared with the single PID controller (Figure 2(b), 2(d)).

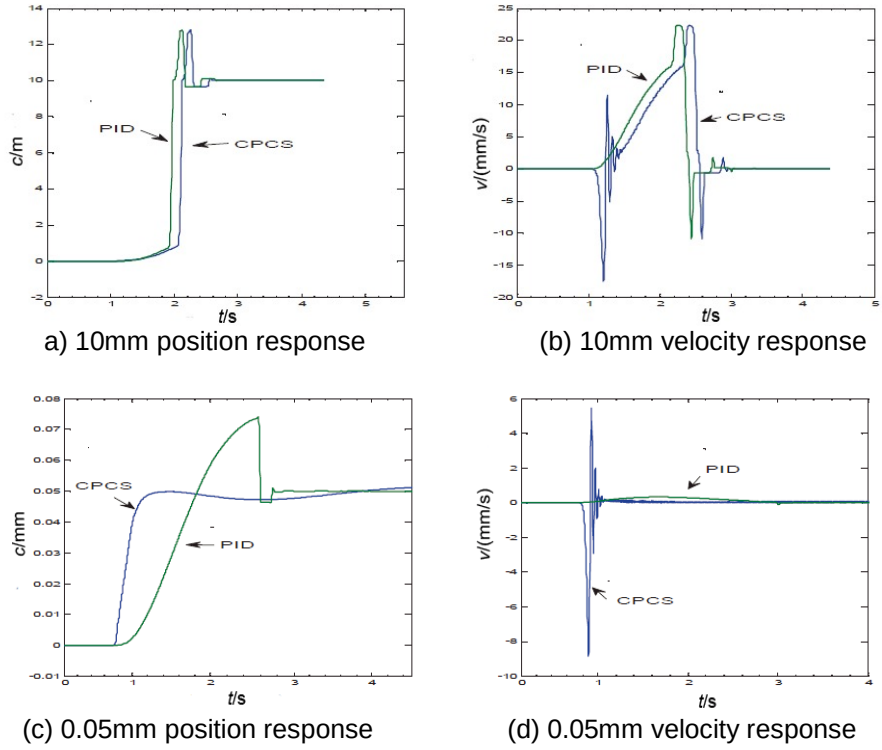

a) 10mm position response (b) 10mm velocity response

(c) 0.05mm position response (d) 0.05mm velocity response

Figure 2. 10mm-0.05mm Positioning Displacement Dynamic Response

2.2. DC Motor Composite Positioning Control System Transfer Function Simplification

In order to explore the correlation between the velocity oscillations and control system internal structure, the root loci of PID and CPCS were analyzed (Figure 3). It was found that PID was an eleventh-order system composed of 5 zeros and 11 poles, and CPCS was a high-order system with 8 zeros and 12 poles. The zero and pole position distributions are shown in Table 1.

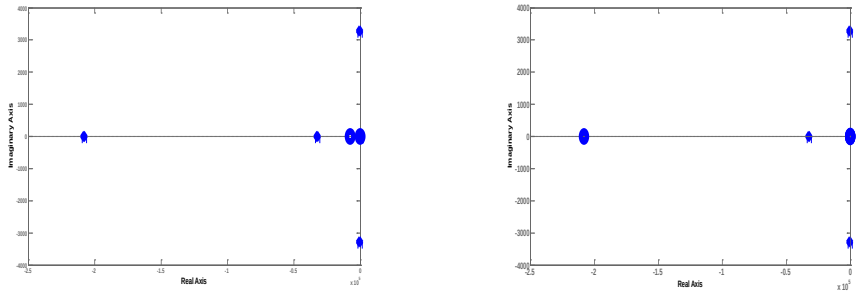

(a) PID Root locus (b) CPCS Root locus

Figure 3. Root Locus of PID and CPCS

Table 1. Poles and Zeros Location of PID and CPCS

PID									
Position	1	2	3	4	5	6	7	8	9
Zero	-3.43	-50	-100	-126	-7.69×10^{3}				
Pole	-4.19	-50	-94.6	-100	-167	$-549\pm3.28\times10^{3}$ j	-3.85±12.8j	-32500	-208000
CPCS									
Position	1	2	3	4	5	6	7	8	9	10
Zero	-0.957	-7.47	-50.9	-92.4	-167	-3.04±6.62j	-2.08×10^{5}			
Pole	-0.957	-6.67	-50	-92,4	-168	-502±3270j	-3.33±6.85j	-195	-32500	-208000

When system gain k was simply given value of 1, the closed-loop transfer functions of PID and CPCS would be:

PID:

$$h(s)=\frac{(s+7690)(s+126)(s+100)(s+50)(s+3.43)}{(s+2.08\times10^{5})(s+3.25\times10^{4})(s+167)(s+100)(s+94.6)(s+50)(s+4.19)(s^{2}+7.7s+178.7)(s^{2}+1098s+1.106\times10^{7})}. \quad (1)$$

CPCS:

$$H(s)=\frac{(s+208000)(s+167)(s+92.4)(s+50.9)(s+7.47)(s+0.957)(s+3.04+6.62i)(s+3.04-6.62i)}{(s+208000)(s+32500)(s+195)(s+168)(s+92.4)(s+49.7)(s+6.67)(s+0.957)(s^{2}+6.66s+58.01)(s^{2}+1004s+1.094\times10^{7})}. \quad (2)$$

Considering that the influence of pairs of poles and zeros at relatively close positions could approximately offset each other and that the impact on the system was weak when poles or zeros were further from the origin [12], formulas (1) and (2) could be simplified using cancellation methods. After further taking into account the compensation of the system gain caused by the simplification [13], we obtained the following results:

PID: $$h(s)=\frac{1.2\times10^{-6}(s+3.43)}{(s+4.19)(s^{2}+7.7s+178.7)(s^{2}+1098s+1.106\times10^{7})}. \quad (3)$$

CPCS: $$H(s)=\frac{2.8\times10^{-5}}{(s+195)(s^{2}+1004s+1.094\times10^{7})}. \quad (4)$$

Figure 4 displays the comparison of closed-loop Bode diagram, position, and velocity responses between the transfer functions of PID ((1) and (3)) and CPCS ((2) and (4)). We found that both systems showed a high degree of consistency with regards to frequency characteristics and dynamic performance before and after the simplification up until the 4000 rad / s frequency range corresponding to its -360^{0} phase angle (PID), and the 10000 rad / s frequency range corresponding to the -270^{0} phase angle (CPCS), both of which are much greater than their operating band ranges.

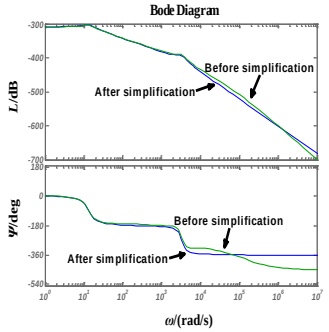

(a) Bode diagram of PID

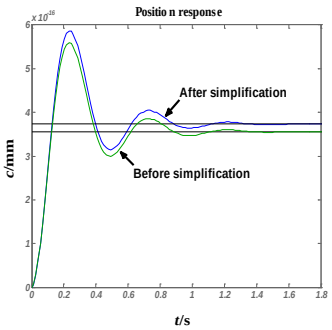

(b) Position response of PID

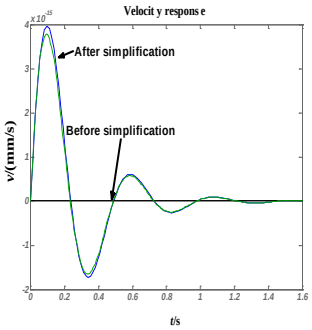

(c) Velocity response of PID

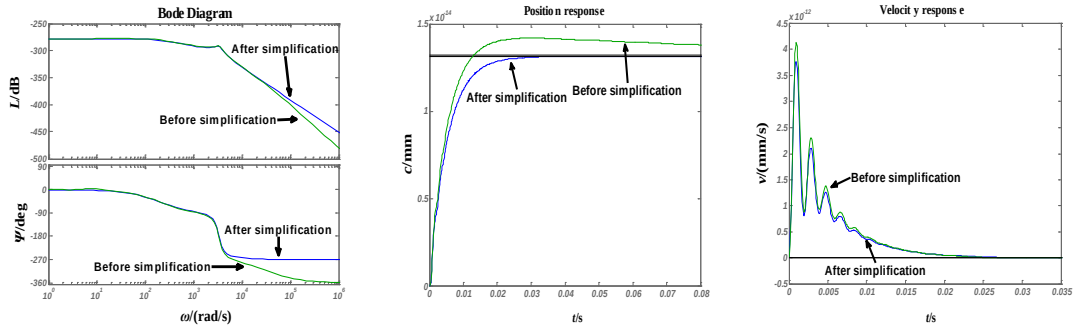

(a) Bode diagram of CPCS (b) Position response of CPCS (c) Velocity response of CPCS

Figure 4. Root Locus, Bode Diagram and Dynamic Response before and after Simplifying of PID and CPCS

Generally, the high-order control system transfer function could be expressed as [14]:

$$G(s) = e^{-ts} \cdot k \frac{(s+z_1)...(s+z_m)}{(s+p_1)...(s+p_m)}. \tag{5}$$

Because the time delay e^{-ts} was a non-minimum phase link, its existence did not affect the zero and pole position distributions [14]. Thus its optimization need not consider its impact, and equation (5) could be translated into:

$$G(s) = k \frac{(s+z_1)...(s+z_m)}{(s+p_1)...(s+p_m)}. \tag{6}$$

Its basic fifth-order simplifying form according to 2.1 would be:

$$h(s) = k' \frac{(s+z)}{(s+p)(s^2+2\xi_1\omega_1 s+\omega_1^2)(s^2+2\xi_2\omega_2 s+\omega_2^2)} \tag{7}$$

Decomposed into typical links:

$$H(s) = \frac{k'z}{p\omega_1^2\omega_2^2} \frac{(1+\frac{1}{z}s)}{(1+\frac{1}{p}s)(\frac{s^2}{\omega_1^2}+\frac{2\xi_1 s}{\omega_1}+1)(\frac{s^2}{\omega_2^2}+\frac{2\xi_2 s}{\omega_2}+1)}. \tag{8}$$

Formula (8) showed that the logarithmic frequency characteristic of high-order control system closed-loop transfer function simplified form could always be the superposition of five typical links, and that all parts were minimum phase links [14].

Comparing formula (3) and (4), we found that during the process of combining PID with PZT to build CPCS: a) the system gain k was increased from 1.2×10^{-6} to 2.8×10^{-5}; b) the real zero was moved from original location of -3.43 left away to infinity; c) the real pole from -4.19 to -195; d) the dominant complex conjugate pole A was moved to infinity; e) the non-dominant complex conjugate poles B's position remained basically unchanged.

CPCS had an obvious difference from PID in both positioning accuracy and stability. These differences in dynamic performance were clearly independent from the change of the system gain [15], which might be caused by the pole and zero position distribution changes.

3. High-order Control System Zero-pole Optimal Configuration

3.1. The Establishment of High-order Control Systems Third-order Dynamic Equation

Analysis of literature [16] regarding the effect of various components in formula (7) on system dynamic performance has led to the following conclusions:

1) The gain *k* only guarantees system steady-state error requirements and does not affect the dynamic performance [12].

2) The location changes of real zeros and poles had no effect on the system stability, and had a minimal impact on the positional accuracy when compared with the dominant complex conjugate pole [16].

3) The non-dominant complex conjugate pole B had no effect on system dynamic performance, but limited the configurable interval [16]. More specifically, when the dominant pole moved within the region, the system dynamic performance was almost entirely determined by the position of A, and when it moved outside the region, the system dynamic performance was primarily determined by B.

Based on 1) and 3) above, we determined that only the real zero, the real pole, and the dominant complex conjugate pole took place in configuration during the high-order control system optimization process. Changes in the system gain, *k*, had no effect on dynamic performance and could therefore be given a value of 1. The non-dominant complex conjugate pole B did not participate in configuration by itself, so it could be reasonably removed from formula (5) and treated as a configurable interval limit. This allowed us to express the system transfer function (7) in the following third order form:

$$h(s)=\frac{(s+z)}{(s+p)(s^2+2\xi_1\omega_1 s+\omega_1^2)}. \tag{9}$$

Its state-space model was:

$$\begin{cases} \dot{x}=\begin{bmatrix}\dot{x}_1\\ \dot{x}_2\\ \dot{x}_3\end{bmatrix}=\begin{bmatrix}0 & 1 & 0\\ 0 & 0 & 1\\ -p\omega_1^2 & -(\omega_1^2+2\zeta_1\omega_1 p) & -(2\zeta_1\omega_1+p)\end{bmatrix}\begin{bmatrix}x_1\\ x_2\\ x_3\end{bmatrix}+\begin{bmatrix}0\\ 0\\ 1\end{bmatrix}u \\ y=\begin{bmatrix}z & 1 & 0\end{bmatrix}\begin{bmatrix}x_1\\ x_2\\ x_3\end{bmatrix} \end{cases}. \tag{10}$$

The high order control system zero-pole optimization problem was then transformed into: (Ⅰ) Seeking the target set *P* of the real zero, the real pole, and the dominant conjugate pole A within the root locus configuration interval defined by the non-dominant conjugate pole B, and according to design specifications, *i.e.* satisfying either the highest positioning accuracy point under a particular stability, or the most stable point under a specific positioning accuracy condition. (Ⅱ) Computing the feedback gain matrix *K* and the estimator gain *L* such that the eigenvalues of formula (10) match the entries of *P*. (Ⅲ) Forming a dynamic regulator or compensator given the state-space model (10), the state-feedback gain matrix *K*, and the estimator gain matrix *L* to optimize system dynamic performance.

Further considering the limited roles of the real pole and the real zero in the system's optimal process according to conclusion 2), we can adopt a two step model to optimize the system: (1) Keeping the real pole and real zero constant, we seek the best target location

distribution of the dominant pole A within the root locus configuration interval to achieve the system optimum. (Ⅱ) We correct results by considering the impact of the real zero, and real pole on the system's dynamic performance.

3.2. Equioscillation and Equiprecision Lines Drawn

The dominant pole was the second-order oscillation link [14]:

$$G(s)=\frac{1}{(s/\omega_n)^2+2\xi(s/\omega_n)+1},\qquad \omega_n>0,0<\xi<1. \tag{11}$$

Its frequency characteristic was:

$$A(\omega)=\frac{1}{\sqrt{(1-\frac{\omega^2}{\omega_n^2})^2+4\xi^2\frac{\omega^2}{\omega_n^2}}}. \tag{12}$$

Taking $dA(\omega)/d\omega=0$, got the resonant frequency:

$$\omega_r=\omega_n\sqrt{1-2\xi^2},\qquad 0<\xi\le\sqrt{2}/2. \tag{13}$$

Formula (13) into (12), obtained the resonant peak:

$$M_r=A(\omega_r)=\frac{1}{\sqrt{2\xi\sqrt{1-\xi^2}}},\qquad 0<\xi\le\sqrt{2}/2. \tag{14}$$

And had the definition of bandwidth frequency substituted into formula (12), we obtained:

$$\omega_b=\omega_n[(1-2\xi^2)+\sqrt{(1-2\xi^2)^2+1}]^{\frac{1}{2}}. \tag{15}$$

The resonant peak M_r and the bandwidth frequency ω_b shown by Eq (14) and (15) had already been proved to be available as the description of system stability and accuracy respectively [16].

When it was expressed with real part *a* and imaginary part *b*, Eq (11) would be:

$$G(s)=\frac{1}{(s-a+bj)(s-a-bj)}. \tag{16}$$

Simultaneous (11) and (16), the congruent relationship between the parameters was obtained:

$$\begin{cases} a=-\omega_n\xi & 1' \\ b=\pm\sqrt{\frac{a^2}{\xi^2}-a^2} & 2' \\ \omega_n=\sqrt{a^2+b^2} & 3' \\ \xi=\sqrt{\frac{a^2}{a^2+b^2}} & 4' \end{cases}. \tag{17}$$

Formula (17) into (14), we received:

$$M_r=\sqrt{\frac{a^2+b^2}{-2ab}}. \tag{18}$$

Equation (18) reflects the correspondence between the system stability (M_r) and the dominant pole position distribution (a, b). When M_r was assigned a different value, we could draw a series of equioscillation lines (equi-M_r) in the root locus configuration interval based on its value.

Similarly, having (17) into (15), we scored:

$$\omega_b = \sqrt{\sqrt{2(a^4 + b^4)} + b^2 - a^2} \ . \tag{19}$$

Equation (19) reflects the relationship between the positioning precision (ω_b) and the position distribution (a, b) of the dominant pole. When ω_b was assigned different values, a series of equiprecision lines (equi-ω_b) could be drawn.

Values of M_r and ω_b are shown in table 2, and equi-M_r and equi-ω_b are plotted on the root locus plane in Figure 5(a) (because of the symmetry relation, only the half plane above the real axis is drawn in the graph). The straight lines through the origin O are equi-M_r, according to the gradient from small to large followed by: equi-M_{r1}, equi-M_{r2}, …,until equi-M_{r16}; and the curves are equi-ω_b, along the $|b|$ increasing direction from down to up order of: equi-ω_{r1}, equi-ω_{r2},…,until equi-ω_{r16}.

Table 2. M_r and ω_b of Equioscillation and the Equiprecision Lines

M_r	M_1	M_2	M_3	M_4	M_5	M_6	M_7	M_8	M_9	M_{10}	M_{11}	M_{12}	M_{13}	M_{14}	M_{15}	M_{16}
Value	1.0	1.2	1.4	1.6	1.8	2.0	2.2	2.4	2.6	2.8	3.0	3.2	3.4	3.6	3.8	4.0
ω_b	ω_1	ω_2	ω_3	ω_4	ω_5	ω_6	ω_7	ω_8	ω_9	ω_{10}	ω_{11}	ω_{12}	ω_{13}	ω_{14}	ω_{15}	ω_{16}
Value	500	1000	1500	2000	2500	3000	3500	4000	4500	5000	5500	6000	6500	7000	7500	8000

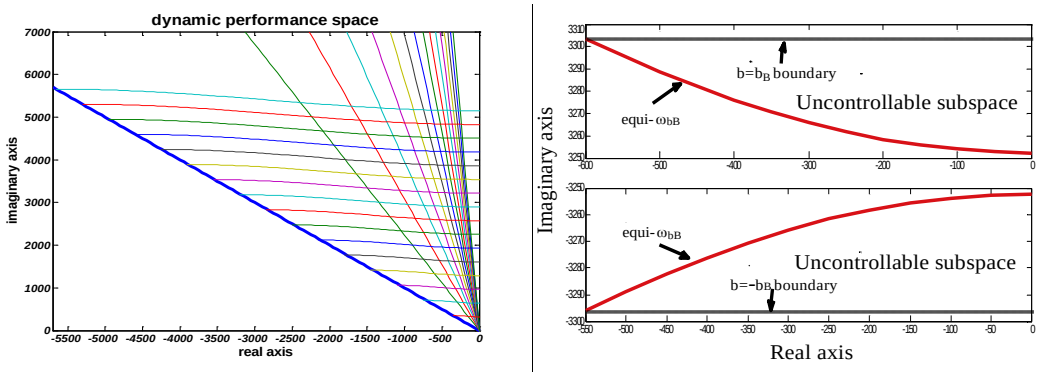

(a) equioscillation and equiprecision lines (b) uncontrollable subspace of PID

Figure 5. Equioscillation, Equiprecision Lines and Subspaces

3.3. Controllable and Observable, Unobservable and Uncontrollable Subspaces

Comprehensive analyses of Table 2 and Figure 5(a) allow us the following conclusions:

1) When the dominant pole moved along any equi-M_r to the lateral relative to the origin, the positioning accuracy was improved despite the system stability being kept constant, dynamic response results are shown in Figure 6(a) and (b); and when the dominant pole moved along any equi-ω_b relative the origin to the lateral, the system positioning accuracy stayed constant and the stability was improved, dynamic response results are also shown in Figure 6(c) and (d).

2) In the configuration interval between the equi-M_r and the equi-ω_b, numbers of "grid" were formed by the intersecting lines. When the dominant pole moved within any grid, the

system's positioning stability and accuracy varied between M_{rn} - $M_{r(n+1)}$ and ω_{bN} - $\omega_{b(N+1)}$ respectively, and when the dominant pole was moved between grids, either positioning accuracy or stability was bound to change. Supposing that the configuration interval was infinitely fractionized by the equi-M_r and equi-ω_b, the grid would fade to location point, It was naturally inferred that system dynamic performance (M_r, ω_b) was uniquely determined by the point coordinates (a, b), forming a fully controllable and observable subspace.

3) In the configuration region between two equi-M_{r1}, the system stability was the same at each point (M_r=1). When the dominant pole was moved along any equiprecision line in the region, there were different positions (a, b) corresponding to the same system dynamic performance (M_r, ω_b), the results of which are shown in Figure 7 (a) and (b). We saw from this case that the system state was not fully reflected by the output, since it formed an unobservable subspace with boundaries (b=±a) that had no relevance with any zero or pole locations.

4) When the dominant pole was shifted into the configuration interval between the boundaries b=$\pm b_B$ and the upper and lower equi-ω_{bB} were as shown in Figure 5 (b), the system positioning accuracy should have been higher than at point B, meaning that there a wider bandwidth frequency should have been generated. This abnormal situation indicated that the non-dominant pole would inevitably incur correlative changes with the dominant pole generated by the uncontrollable state. In addition, the uncontrollable subspace's boundaries were clearly determined by only the non-dominant complex conjugate pole. The dynamic response results are shown in Figure 7 (c) and (d).

The configuration results for moving the dominant pole along any equi-M_r within the controllable and observable subspace are shown in Figure 6(a), (b). The position of each point was selected as follows: A (a = -3.84, b = 12.8), E (a = -185.28, b = 784.36), F (a = -367.28, b = 1552.49) and D (a = -549, b = 2320). It can be seen from the Bode graph in Figure 6(a) that all curves had the same resonant peak size despite an increasing bandwidth frequency. This corresponds to the velocity response in Figure 6(b), which shows that system stability stayed constant, but positioning accuracy improved successively.

When the dominant pole moved along any equi-ω_b, we selected points with the following values: G (a = -150, b = 2383), H (a = -300, b = 2396), M (a = -450, b = 2417), and D (a = -550, b = 2435). The Bode diagram and velocity response curves are shown in Figure 6 (c), (d). From that figure it can be seen that each curve has almost the same bandwidth frequency, and the gradually decreasing resonant peak size (Figure 6 (c)), corresponds to the improving system stability and the constant positioning precision (Figure 6 (d)).

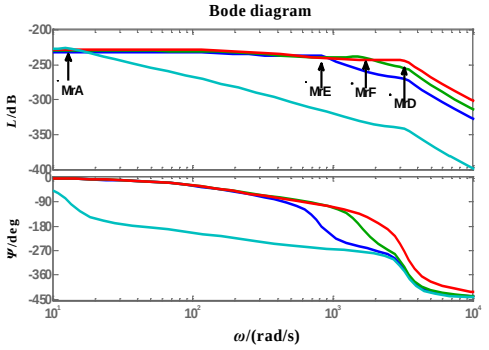

(a) Bode diagram comparison on equi-M_r

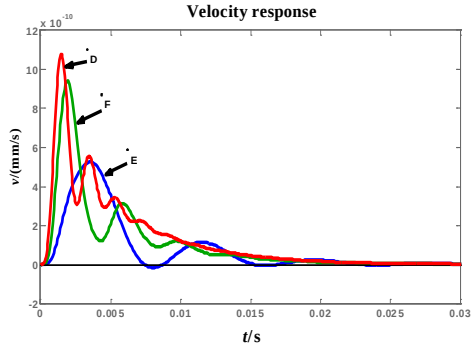

(b) Dynamic response comparison on equi-M_r

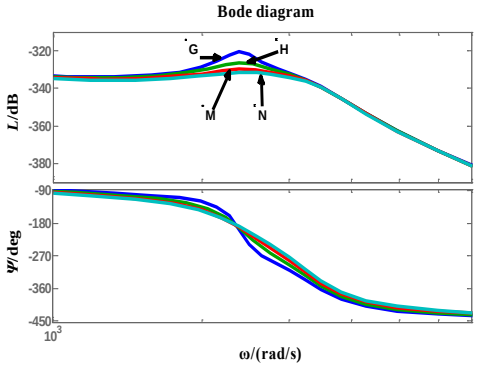

(c) Bode diagram comparison on equi-ω_b

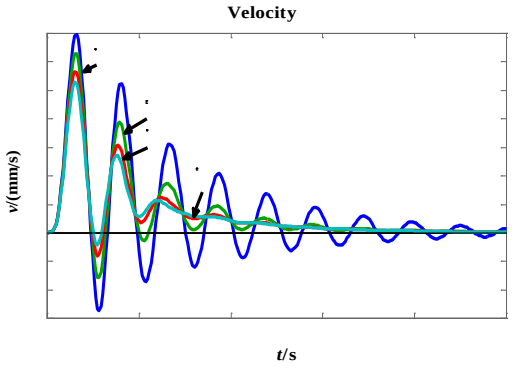

(d) Dynamic response comparison on equi-ω_b

Figure 6. Bode Diagram and Dynamic Response within Controllable and Observable Subspace

Figure 7 (a), (b) shows the Bode diagram and the dynamic performance comparisons when the dominant pole was moved along any equi-ω_b in the unobservable subspace. The values of the points selected were: O (a = -200, b = 52.38), P (a = - 300, b = 68.37), Q (a = -400, b = 76.30) and R (a = -500, b = 88.45). It was detected that although position distribution changes between points were large, the resonance peaks, bandwidth frequencies, positioning accuracies, and system stabilities were basically the same, reflecting that different position distributions corresponded to similar dynamic performance within the subspace.

The Bode diagram and dynamic performance for the dominant pole moving in the uncontrollable subspace are shown in Figure 7 (c), (d). All selected points are as follows: B (a = -549, b = 3280), S (a = - 300, b = 3260) and T (a = -100, b = 3240). From the Bode diagram in 7 (c), we found that even though the dominant pole remained in the configuration region, its resonance peak disappeared, meaning that only the non-dominant pole's, B, single resonance peak appeared on the frequency resonance curve. This told us that a) the underlying frequency of the resonant peak was completely identified by the non-dominant complex conjugate pole, having no relevance to the dominant pole, and b) the size of the resonant peak was wholly determined by the position distribution of the dominant pole, being independent of the non-dominant pole B. Velocity response curves are shown in Figure 7 (d), and it was discovered that when the dominant pole moved from B to T along the line BT, the system stability reduced. However, the accuracy did not change accordingly, indicating that the region was surprisingly displayed as an "equi-precision" area, and that the correspondence between the dominant pole position distribution and the positioning accuracy disappeared there, appearing in the uncontrollable state.

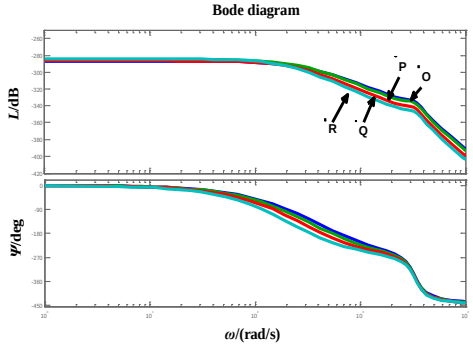

(a) Bode diagram on equi-ω_b in unobservable subspace

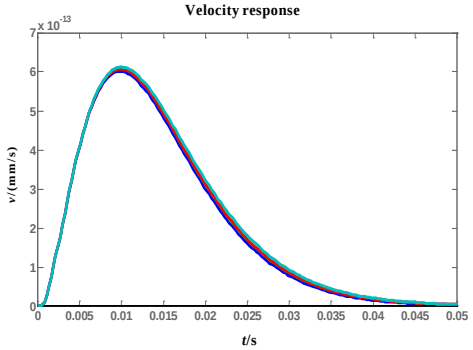

(b) Dynamic response on equi-ω_b in unobservable subspace

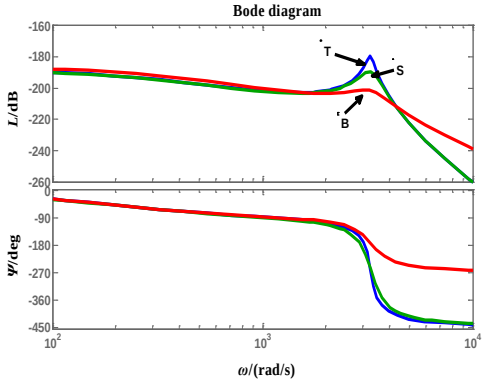

(c) Bode diagram on equi-ω_b in uncontrollable subspace

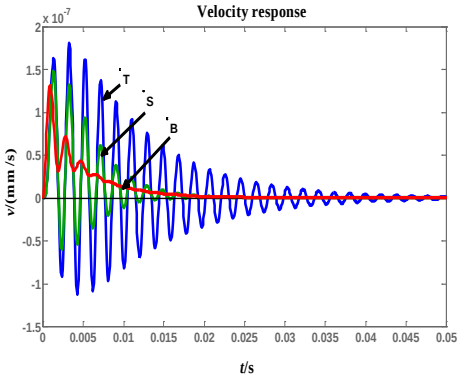

(d) Dynamic response on equi-ω_b in uncontrollable subspace

Figure 7. Bode Diagram and Dynamic Response within Uncontrollable and Unobservable Subspace

3.4. High-order Control System Dominant Complex Conjugate Pole Optimal Configuration

Figure 8 (a) shows the comparison of PID and CPCS root loci. It was found that during the process of combining PID and PZT to build CPCS, the dominant pole had not been configured within the controllable and observable subspace, but rather moved along the greater slope equi- M_r line into the uncontrollable subspace, resulting in CPCS having greater oscillations and almost the same accuracy as at point B (Figure 8 (b) speed response curves). This appears in the result shown in Figure 2.

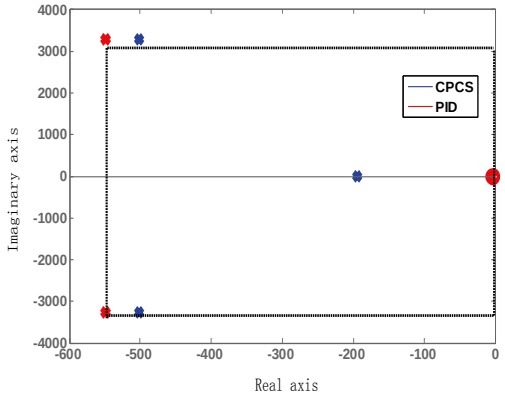

(a) Root locus comparison between PID and CPCS

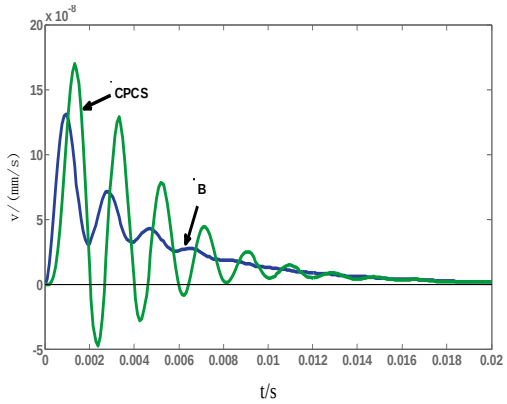

(b) Dynamic response comparison of CPCS and point B

Figure 8. Root Locus and Dynamic Response of CPCS

Taking the CPCS transfer function (4), its state-space model is the plate G:

$$G=\begin{cases}\dot{x}=\begin{bmatrix}-195 & 0.01749 & 0\\ 0 & -502 & 3269\\ 0 & -3269 & -502\end{bmatrix}\begin{bmatrix}x_1\\ x_2\\ x_3\end{bmatrix}+\begin{bmatrix}0\\ 0\\ 5.465\times10^{-4}\end{bmatrix}u\\ y=\begin{bmatrix}8.96\times10^{-4} & 0 & 0\end{bmatrix}\begin{bmatrix}x_1\\ x_2\\ x_3\end{bmatrix}\end{cases}. \quad (20)$$

We tried to keep CPCS' real zero and real pole positions unchanged, and to configure the dominant pole from the original position, (502±6358.5i), to point B, (549±3286.03i), by building a positive feedback regulator as shown in Figure 9, in order to realize the optimization of the system's dynamic performance.

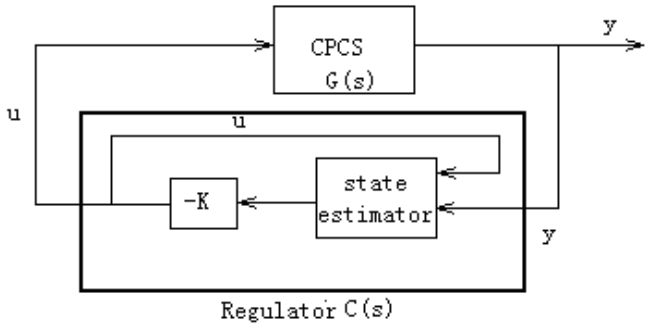

Figure 9. Regulator of CPCS

1) The vector P of desire self-conjugate close-loop pole location was then: P=[-195, 549+3286.03i, 549-3286.03i];

2) Computed the gain matrix K such that the eigenvalues of

$\begin{bmatrix}-195 & 0.01749 & 0\\ 0 & -502 & 3269\\ 0 & -3269 & -502\end{bmatrix}-\begin{bmatrix}0\\ 0\\ 5.465\times10^{-4}\end{bmatrix}K$ matched the entries of P:

.K=[0, 0.6798×10^{6}, -3.8460×10^{6}]

3) We could also compute the estimator gain L such that the eigenvalues of

$\begin{bmatrix}-195 & 0 & 0\\ 0.01749 & -502 & -3269\\ 0 & 3269 & -502\end{bmatrix}-\begin{bmatrix}8.96\times10^{-4}\\ 0\\ 0\end{bmatrix}L'$ matched the entries of P:

$$L=\begin{bmatrix}0\\ 1.1869\times10^{11}\\ 4.3125\times10^{11}\end{bmatrix}.$$

4) Formed the dynamic regulator C given the state-space model (20) of the plate, the state-feedback gain matrix K, and the estimator gain matrix L:

$$C=\begin{cases}\dot{x}=\begin{bmatrix}1907 & 0.01479 & 0\\ -1.063\times10^{8} & -502 & 3269\\ -3.864\times10^{8} & -3641 & 1600\end{bmatrix}\begin{bmatrix}x_1\\x_2\\x_3\end{bmatrix}+\begin{bmatrix}-2.346\times10^{6}\\1.187\times10^{11}\\4.312\times10^{11}\end{bmatrix}u\\ y=\begin{bmatrix}-1.136\times10^{-4} & -6.798\times10^{5} & 3.846\times10^{6}\end{bmatrix}\begin{bmatrix}x_1\\x_2\\x_3\end{bmatrix}\end{cases}. \quad (21)$$

The closed-loop H_∞ optimal cost of Figure 9 was:

$$\gamma=b(G,C)=\frac{1}{\left\|\begin{bmatrix}I\\C\end{bmatrix}(I+GC)^{-1}[G,I]\right\|_\infty}=1.84 \quad . \quad (22)$$

This gives a good indication of robustness of stability to a wide class of unstructured plant variations [17].

Figure 10 shows CPCS' positioning effect on the position continuously changing mobile after configuring the dominant pole to location B. Figure 10 (a) displays the dynamic response curves and Figure 10 (b) shows a 5s-10 s partial enlarged view. It was clearly seen that to the continuously position changing mobile, the optimized CPCS' position response remained consistent with the signal changes, and both overshoot and maximum positioning time were significantly less than those of PID, meaning that CPCS could preferably solve the discrepancy between the positioning accuracy and time delay, and meet the exact dynamic tracking requirement, giving an effect far better than any kind of single PID controller.

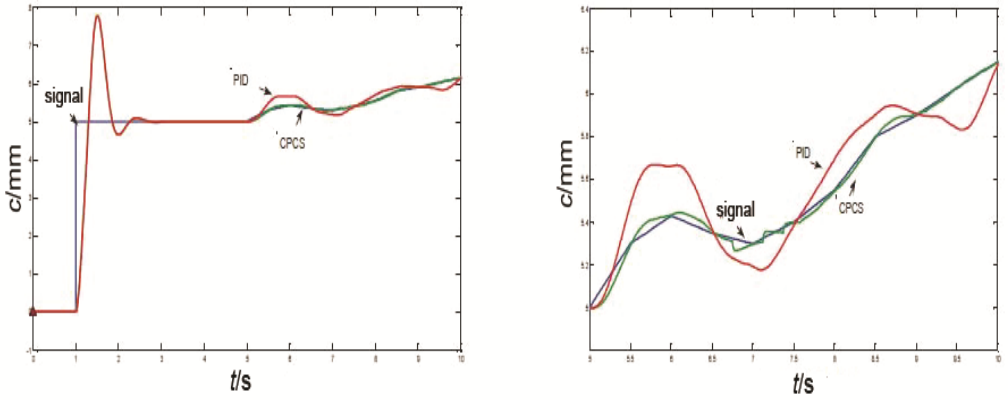

(a) Whole dynamic response curve (b) 5 s-10 s partial enlarged view

Figure 10. System Dynamic Response Comparison of PID and CPCS in the Dynamic Positioning Process

3. 5. High-order Control System Real Zero Pole Optimal Configuration

As was mentioned before, our previous systematic studies have shown the effect of real zero and pole position distribution changes to systematic dynamic performance in literature [16]. However, no distinct evidence was found about their pivotal role in the optimal configuration process. Therefore, we deduced that their function might only be to fine tune the system dynamic performance, and maintain the balance of the system internal structure. If so, further research will be done in the future.

4. Conclusion

This article divided the high-order control system root locus configuration interval into controllable and observable, and uncontrollable and unobservable subspaces by introducing equioscillation and equiprecision lines. Bode diagram and dynamic response results showed that simplifying the transfer function to its fifth-order form using the zero and pole elimination method, and further ignoring the influence of the real poles and zeros on system dynamic properties did not change the subspaces' controllability and observability. Accordingly, the determination of the high-order control system status feedback gain matrix and estimator gain can be converted to the solution on the third-order state or dynamic equation under specific boundary conditions and the original state. This conclusion could effectively solve the contradiction between positioning accuracy and system stability, preferably achieving the optimal configuration, and having significance in improving high-order control system dynamic performance.

Acknowledgements

We thank Peng Wu and Fang Chen for their technical support, help, and fruitful discussions. Xu-yun Chen and Paul Yuan are kindly acknowledged for the language modification. This work was supported by grants from the Anhui province educational development for Natural Scientific Key Research Project (KJ2014A256).

References

[1] L. H. Dou, L. X. Dong, M. Chen and Y. Q. Xia, "Predictive control for mechanical system with backlash based on hybrid model", Journal of Systems Engineering and Electronics (English), vol.20, no.1, **(2009)**, pp. 1301-1308.
[2] S. H. Li, H. X. Liu and S. H. Ding, "A speed control for a PMSM using finite-time feedback control and disturbance compensation", Transactions of the Institute of Measurement and Control, vol. 32, no.2, **(2010)**, pp. 785-789.
[3] J. Chen, Z. F. He and X. Qi. "A new control method for MIMO first order time delay non-square system", Journal of Process Control, vol. 21, no. 4, **(2011)**, pp. 538-546.
[4] X. Lin, S. X. Pan and D. Y. Wang, "Dynamic simulation and optimal control strategy for a parallel hybrid hydraulic excavator", Journal of Zhejiang University Science A, vol. 9, no. 5, **(2008)**, pp. 624-632.
[5] X. Yu and Z. Man, "Fast terminal sliding mode control design for nonlinear dynamic systems", IEEE Trans. Circuits Systems Part 1, vol. 39, no. 2, **(2002)**, pp. 261-264.
[6] G. Kerschen, K. Worden, A. F. Vakakis and J. C. Golinval, "Past, present and future of nonlinear system identification in structural dynamics", Mechanical Systems and Signal Processing, vol. 20, no. 3, **(2006)**, pp. 505-592.
[7] T. Bakhtiar and S. Hara, "H_2 regulation performance limitations for SIMO linear time-invariant feedback control systems", Automatica, vol. 44, no. 3, **(2008)**, pp. 659-670.
[8] X. D. Chen and C. Q. Zhang, "Research on the composite positioning control system of DC motor", Piezoelectrics and Acoustooptics, vol. 34, no. 5, **(2012)**, pp. 788-791.
[9] X. J. Rui and Y. Z. Zhong, "Experiment research on the properties of piezoelectric ceramic Microactuators", Acta Aeronautica Et Astronautica Sinica**,** vol. 16, no. 3, **(1995)**, pp. 299-303.
[10] Y. T. Liu, R. F. Fung and T. K. Huang, "Dynamic response of a precision positioning table impacted by a soft-mounted piezoelectric actuator", Precision Engineering, vol. 28, no. 3, **(2004)**, pp. 252-260.
[11] Y. M. Zhao, W. F. Xie and X. W. Tu, "Performance-based parameter tuning method of model-driven PID control systems", ISA Transactions, vol. 51, no. 3, **(2012)**, pp. 393-399.
[12] S. S. Hu, "Principles of automatic control (Fourth edition)", Science Press, Beijing, **(2005)**.
[13] S. K. Dwivedy and P. Eberhard, "Dynamic analysis of flexible manipulators, a 1iterature review", Mechanism and Machine Theory, vol. 41, no. 7, **(2006)**, pp. 749-777.
[14] C. D. Richard and H. B. Robert, "Modern contro1 system", Addison-Wesley Longman Publishing Co., Inc., Boston, MA, USA, **(1995).**
[15] F. H. Sun, Z. Q. Sun and P. Y. Woo, "Neural network-based adaptive controller design of robotic manipulators with an observer", IEEE Transactions on Neural networks, vol. 12, no. 1, **(2001)**, pp. 54-67.

[16] X. D. Chen and P. Feng, “The Performance analysis and system optimization of the composite position control system of DC motor”, Chinese Journal of Engineering Design, vol. 19, no. 5, **(2012)**, pp. 391-399.
[17] D. C. McFarlane and K. Glover, "A Loop Shaping Design Procedure using Synthesis," IEEE Transactions on Automatic Control, vol. 37, no. 6, (**1992**), pp. 759– 769.

Authors

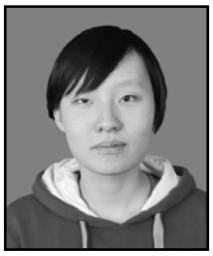

Xiaoxuan Chen, she was born in Anhui, China, in 1995. She is currently pursuing the B.D. degree of chemical engineering at College of Chemistry and Chemical Engineering, Shihezi University. Her main research interests include harmonic elimination, motor drive, intelligence control systems and chemical engineering.

Xudong Chen, He received the M.S. degree in physics from University of Science and Technology of China, Hefei, China, in 2006. He is currently an assistant professor in physics in Anhui Press and Publication Vocational College. His main research interests include high-order control system, harmonic elimination, artificial intelligence applications, motor drive, and intelligence control systems.